Atomic-resolution observations of silver segregation in a [111] tilt grain boundary in copper

Lena Langenohl,[1,*] Tobias Brink,[1,*,†] Gunther Richter,[2] Gerhard Dehm,[1,‡] and Christian H. Liebscher[1,§]
[1]*Max-Planck-Institut für Eisenforschung GmbH, Max-Planck-Straße 1, 40237 Düsseldorf, Germany*
[2]*Max Plank Institute for Intelligent Systems, Heisenbergstraße 3, 70569 Stuttgart, Germany*

(Received 5 December 2022; accepted 31 March 2023; published 20 April 2023)

Alloying a material and hence segregating solutes to grain boundaries is one way to tailor a material to the demands of its application. Direct observation of solute segregation is necessary to understand how the interfacial properties are altered. In this study, we investigate the atomic structure of a high-angle grain boundary both in pure copper and upon silver segregation by aberration-corrected scanning transmission electron microscopy and spectroscopy. We further correlate the experiments to atomistic simulations to quantify the local solute excess and its impact on grain boundary properties. We observe that the grain boundary structure remains intact upon silver segregation and up to five different positions within a structural unit serve as segregation sites. By combining the atomic-resolution observation with atomistic modeling, we are able to quantify the local silver concentration and elucidate the underlying segregation mechanism.

DOI: 10.1103/PhysRevB.107.134112

I. INTRODUCTION

Segregation of elements to grain boundaries (GBs) has a dramatic impact on material properties. Examples include the material becoming stronger, or generally having a more stable microstructure [1–7], but also increasing the susceptibility to failure through corrosion or embrittlement [8–10]. One of the most prominent examples of embrittlement is alloying bismuth to copper, which was already discovered back in 1874 [11]. More recent publications explain the embrittlement by a weakening of the metallic bonds at the GB, which can be related to a pure atomic size effect or the change of the electronic structure at the GB [12–14].

Early research on segregation revealed significant changes in segregation behavior for GBs with different misorientations between both grains using autoradiographs, atomic absorption spectroscopy, or Auger electron spectroscopy [15–18]. Even though such techniques can reveal chemical changes by less than 1 at-% and the spatial resolution across the GB can go down to 0.1 nm, the lateral resolution, revealing chemical changes within the GB structure, is impossible. Furthermore, it was already stated a long time ago that also other GB parameters and thus the existing GB and its atomic structure should play a crucial role, even though experimental observations on the atomic scale were not available [19–23]. Segregation can change different properties of the existing GB phase, such as its mobility, energy, stability, but also its atomic structure [24]. It can introduce mono- or bilayers [12,25,26] or precipitates of solute atoms at the GB, and can even change the GB plane by faceting or induce a GB phase transformation [27–30]. Only a few direct experimental observations of segregation at the GB on the atomic level exist so far since high-resolution imaging microscopes and spectroscopy are needed [4,12,29–36]. To completely comprehend how segregation affects macroscopic features, such as strengthening, embrittlement, or corrosion, we must first identify the segregation-induced atomistic changes inside a GB structure.

The fundamental thermodynamics implemented by Gibbs can be used to describe adsorption at interfaces. Langmuir and McLean used these equations to develop a model of GB segregation, describing the concentration limit of solutes at the GB in dependence of the bulk concentration and temperature [37]. Their model combines thermodynamics with statistical mechanics, using a finite number of atomic positions in the GB which can be completely replaced by solute atoms [37]. Since it is based on mean-field theory, only a single value of GB segregation concentration can be calculated and it does not take into account site-specific changes of concentrations within the GB structure. It neglects interactions between individual atoms, which can significantly contribute to the segregation behavior [38]. Guggenheim and Fowler extended the segregation model, taking into account the interaction between neighboring atoms and the probabilities of neighboring atoms being a solute or matrix element [39]. Recently, more and more attention was paid to site-specific segregation within the GB structure [40–44]. To provide evidence for thermodynamic models that take this into account, experimental observations are needed to validate the theoretically calculated GB structure itself and the segregational site occupancies [23].

*These authors contributed equally to this work.
†t.brink@mpie.de
‡dehm@mpie.de
§liebscher@mpie.de

Due to its high conductivity, Cu is used in many electronic applications and long-pulse high-field magnets [45]. But because Cu is also quite soft and would not sustain the electromagnetic forces, alloying different elements is a common technique to increase its tensile strength which needs to be balanced with an undesired concomitant decrease in conductivity [46]. When alloying Ag to Cu, an increase in tensile strength can be observed [7,47]. Upon specific heat treatments, it can be accompanied by a high conductivity of $\geqslant 80\%$ IACS (International Annealed Copper Standard) [48–50].

Even though Cu–Ag alloys are promising materials, very few experimental studies reveal the segregation of elements at the GB on an atomistic level [29,30]. Divinski *et al.* [51] investigated the diffusion behavior of Ag in Cu $\Sigma 5$ GBs and observed abrupt changes in diffusivity at elevated temperatures, attributed by Frolov *et al.* to a GB phase transformation [52]. Simulation studies on Cu–Ag systems can explain the underlying atomistic effects [7,26,47,52,53]. However, experimental observations are needed to confirm the atomistic changes and structures at the GB. Cu–Ag is a good model system to study segregation at GBs due to its extended miscibility gap and absence of intermetallic phases [54].

Here, we investigate Ag segregation at a $\Sigma 37c$ $\langle 111 \rangle$ $\{347\}$ GB at atomic resolution using aberration corrected scanning transmission electron microscopy (STEM) combined with atomically resolved energy dispersive x-ray spectroscopy (EDS) and hybrid molecular dynamics (MD)/Monte Carlo (MC) simulations. We show different methods for correlating experimental observations with simulations and investigate the evolution of Ag segregation as a function of its concentration. Finally, we discuss different parameters which may be responsible for the site occupation of Ag within a high-angle GB.

II. METHODS

A. Experimental specimen preparation and STEM investigation

A Cu thin film was deposited on a $\langle 0001 \rangle$ sapphire wafer by the Central Scientific Facility Materials of the Max Planck Institute for Intelligent Systems in Stuttgart. The Al_2O_3 substrate was sputter cleaned at 200 eV for 5 min and subsequently annealed at 1000 °C for 1h. In a next step, a 2-μm-thick layer of Cu was deposited at room temperature by molecular beam epitaxy (MBE) with a rate of 0.3 nm/s. After deposition, the film was annealed for 2 h at 450 °C inside the same chamber. For the investigation of Ag segregation, 100 nm of Ag were sputtered on top of the film at the Ruhr-Universität Bochum. Prior to that, the top oxide layer was removed by Ar^+ sputtering. Consecutively, the film covered with Ag was annealed at 600 °C for 16 h. For comparison, one part of the same film was annealed at 600 °C for 16 h without a Ag layer. Both films, with and without Ag, were characterized using a Thermo Fisher Scientific Scios2HiVac dual-beam secondary electron microscope (SEM) equipped with an electron-backscattered diffraction (EBSD) detector. Inverse pole figure (IPF) maps of the EBSD scans helped to identify the GBs of interest, which were then lifted out using a focused Ga^+ ion beam (FIB). The initial milling of the FIB sample was performed with relative tilts of the sample by ±3° away from the FIB axis and an ion voltage of 30 kV and current of 100 pA. Once the sample was ∼300 nm thin, the tilt angles were reduced to ±1°–2° and the current was reduced to 50 pA. For the final polishing steps, when the sample reaches a thickness of ∼100 nm, the tilt angles were again increased to ±7°. At the same time, the ion acceleration voltage was reduced from 30 to 5 kV and the current was lowered from 50 to 16 pA and later 7.7 pA for final milling down to a thickness of about 40 to 80 nm.

The FIB lamellas were then inspected using a probe-corrected FEI Titan Themis 80-300 (Thermo Fisher Scientific) (scanning) transmission electron microscope ((S)TEM). The TEM is equipped with a high-brightness field emission gun, set to a voltage of 300 kV and a probe current of 70–80 pA for imaging. A high-angle annular dark-field (HAADF) detector (Fishione Instruments Model 3000) was used to record the HAADF-STEM datasets with collection angles of 78–200 mrad and a semiconvergence angle of 17 mrad. EDS measurements were performed at 120 kV and acquired for at least 15 min. As we registered a 120 kV STEM-HAADF image along with the EDS measurement and wanted to ensure atomic resolution, a fine scan step size of 512×172 px with a pixel size of 14.47 pm was chosen. For the EDS intensity, subsequent binning of 4×4 pixels was needed to obtain sufficient data for each position. An additional Gaussian filter was used to make intensity changes in the Ag L-α peak more visible, ensuring at the same time that the main findings stayed unaffected.

Raw data for the experiments is available in the companion dataset [55].

B. MD/MC simulations

We used LAMMPS [57,58] with an embedded atom method (EAM) potential for Cu–Ag by Williams *et al.* [59] for all simulations. In a first step, a bicrystal containing the experimentally observed GB was obtained by joining two copper face-centered cubic (fcc) crystals to produce a $\Sigma 37c$ GB with $[\bar{1}11]$ tilt axis and $(\bar{3}\bar{7}4)$ and $(3\bar{4}7)$ GB planes, respectively. We varied the relative displacements between the crystallites followed by minimization of the potential energy until the experimentally observed structure was found (γ-surface method). The final system was approximately of size $94 \times 81 \times 187$ Å^3 with 119 880 atoms. We applied open boundaries normal to the GB and otherwise periodic boundary conditions.

In a second step, we computed the bulk silver concentration. Alloying was simulated in an isobaric semi-grand-canonical ensemble by hybrid MD/MC simulations [60], defined by the total number of atoms N, pressure $p = 0$ Pa, temperature T, and chemical potential difference $\Delta\mu = \mu_{Ag} - \mu_{Cu}$. The latter controls the concentration of silver. MD time integration with a time step length of 2 fs was alternated with $0.1N$ MC trial steps every 20 MD time steps. The bulk silver concentration was computed by running the simulations with $\Delta\mu$ from 0.3 to 1.0 eV at 300 and 500 K on a fully

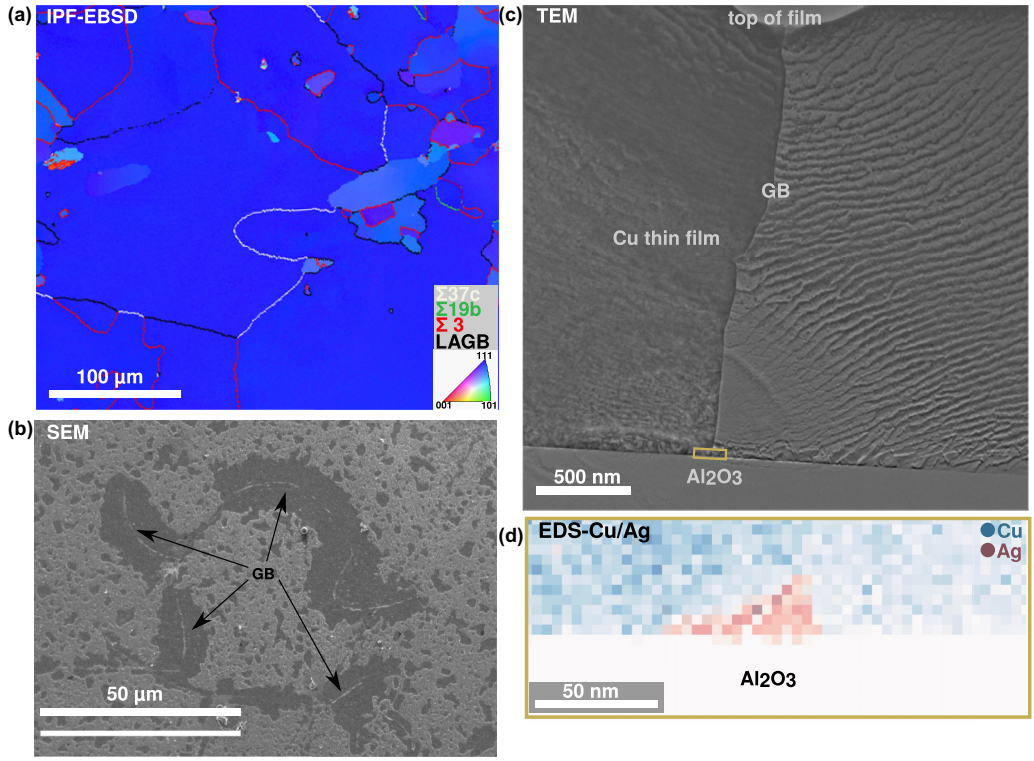

FIG. 1. Characterization of the film with and without Ag. (a) EBSD of the microstructure of the pure Cu film. (b) SEM image of the surface of the film after Ag deposition and annealing. (c) Bright-field TEM image of a cross section of a Σ37c GB of the Cu thin film with Ag. Minor striations, which can be seen in the right grain, are most likely surface artifacts from FIB sample preparation [56]. (d) EDS map from the interface of the GB with the substrate shows a Ag precipitate at the bottom, which signifies that Ag diffused entirely across the GB down to the substrate.

periodic system of 32 000 atoms ($20 \times 20 \times 20$ unit cells) of fcc copper for 10 ns.

Finally, we simulated the segregation of silver to the GBs. To avoid size effects due to the excess GB stress [61], we fixed the sizes of the systems containing the GBs in the periodic directions using the lattice constant of the pure copper system at the given temperature, thus switching to the standard isochoric semi-grand-canonical ensemble. This is a reasonable approximation due to the very low solubility of Ag in Cu, meaning that the lattice constant is not a function of $\Delta\mu$. The lattice constants were obtained by equilibrating a periodic, pure fcc Cu system in the isothermal–isobaric ensemble for 250 ps. Then, the system containing the GB was scaled to the correct lattice constant and equilibrated in the semi-grand-canonical ensemble for 20 ns with the same parameters as above. At 300 K we used $\Delta\mu$ values from 0.30 eV (almost pure copper) to 0.74 eV (phase transition to silver at 0.72 eV). At 500 K we used $\Delta\mu$ values from 0.40 eV (very low silver concentration) to 0.68 eV (GB starts to disorder). Excess properties were calculated as defined in Refs. [61,62] and simulation results were visualized with OVITO [63]. The Ag occupation of atomic columns as viewed from the tilt axis direction was calculated by averaging over an MD/MC simulation running for an MD time of 1 ns.

Raw data for the simulations is available in the companion dataset [55].

III. RESULTS AND DISCUSSION

A. Microstructure of the investigated thin film

We studied the global thin film microstructure and grain boundary evolution by EBSD and TEM combined with EDS before and after Ag segregation. An inverse pole figure map of the electron backscattered diffraction dataset of the pure Cu thin film is shown in Fig. 1(a). The out of plane orientation of most grains is close to ⟨111⟩ as expected for Cu on a single crystalline ⟨0001⟩ Al_2O_3 wafer [64,65]. The {111} ⟨0$\bar{1}$1⟩ direction of the Cu film is oriented parallel to the (0001) ⟨2$\bar{1}\bar{1}$0⟩ direction of the α-Al_2O_3 substrate as was already observed in other Cu thin films grown on sapphire [65]. The grain size varies between several µm up to more than 200 µm, all of them being larger than the film thickness (2 µm). The thin film was then divided into several pieces. One piece was annealed at 600 °C for 16 h and no further grain growth could be observed (see Figs. S1(a) and S1(b) in the Supplemental Material (SM) [66]). On another piece we deposited a 100 nm layer of Ag. Subsequent annealing under the same condition as for the piece without Ag deposition let Ag diffuse along the GBs. An SEM image of the film after Ag deposition and annealing is shown in Fig. 1(b). Ag is still present in most areas of the film (here visible in brighter colors), whereas some grooved GBs show a Ag-depleted zone around the GB (indicated by arrows). To verify that Ag diffused along the complete GB, a cross section of a Σ37c GB was investigated by TEM [Fig. 1(c)] and EDS [Fig. 1(d)]. A Ag precipitate was

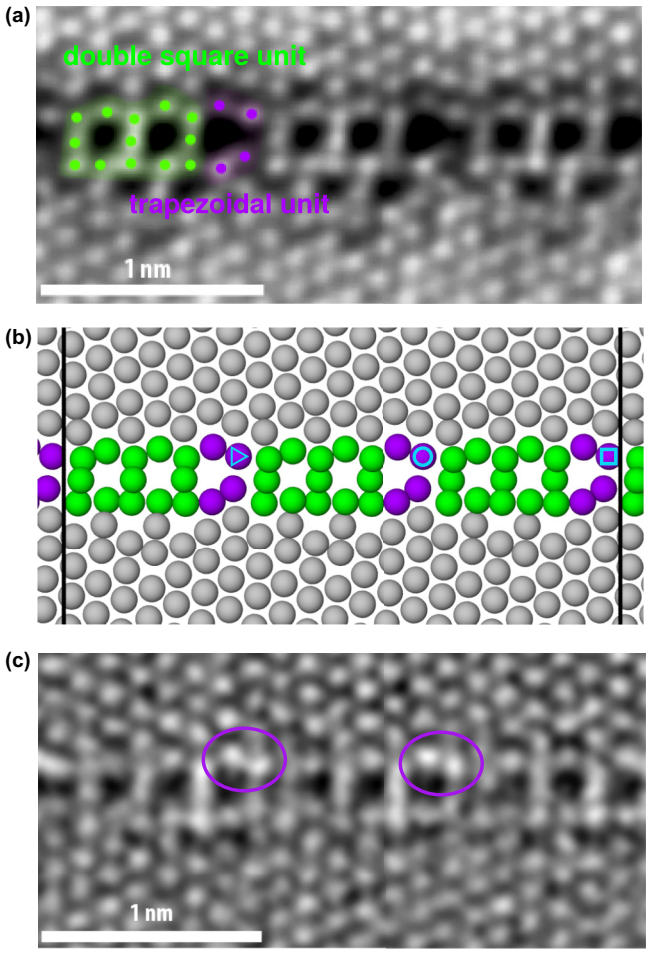

FIG. 2. The atomic structure of a Σ37c ⟨111⟩ {347} GB. (a) HAADF-STEM image at 300 kV of a GB with a misorientation of $(50.9 \pm 0.3)^\circ$ in the pure Cu film. (b) MD model of the zipper structure in pure Cu. The vertical lines indicate the unit cell. The triangle, circle, and square symbols in petrol show CSL points in different positions along the tilt axis direction. (c) HAADF-STEM image at 300 kV of a GB with a misorientation of $(50.9 \pm 0.3)^\circ$ from the Ag segregated Cu film.

observed at the interface between the Al_2O_3 substrate and the Cu film at the GB indicating that Ag diffused along the GB for the entire film thickness.

B. Observations of the GB structure with and without Ag

In a next step, the atomic structure of the grain boundary and the influence of Ag segregation to it were investigated. Figure 2(a) shows an atomically resolved HAADF-STEM image of a Σ37c ⟨111⟩ {347} GB in pure Cu with a misorientation of $(50.9 \pm 0.3)^\circ$. For comparison, the exact misorientation of a Σ37c ⟨111⟩ GB is 50.57° [67]. The experimentally obtained misorientation angle is an average of at least 10 different measurements of angles between different ⟨220⟩ planes of both grains. The bright spots can be directly correlated to atomic columns. The GB structure can be described by the structural unit model [68] and divided into two alternating subunits: One double-square unit, consisting of 13 atomic columns, and one trapezoidal unit with four atomic columns. The same atomic arrangement was found in the pure Cu film after annealing (see Fig. S1(d) in the SM [66]). Atomistic simulations of the same GB also exhibit the same atomic structure [Fig. 2(b)]. The total length of the repeating GB structure with both subunits is equivalent to the length of one third of a Σ37c ⟨111⟩ {347} coincidence site lattice (CSL) unit cell. The CSL of the investigated GB is shown in Fig. S2 in the SM [66]. After one third, the CSL shows a coincidence site, which is at a different position along the tilt axis direction than the first coincidence site, as indicated by different symbols in Fig. S2 in the SM [66]. The coincidence lattice sites are as well indicated in petrol in Fig. 2(b). In general, a multiple of the length of the repeating GB structure should always be equal to the length of the CSL cell (or an integer multiple of it; in our case we have three repetitions in the CSL cell), allowing the repeating GB structure to exist within the repeating CSL. Otherwise, the strain field and coincidence sites would always change and a repeating pattern within the GB would be impossible. The subunits of the Σ37c ⟨111⟩ {347} GB are similar to the Σ19b ⟨111⟩ {235} GB [28], in which the misorientation angle between both grains is 46.8°. In that case, a single square instead of a double-square unit alternates with the same trapezoidal unit as observed in our case. When increasing the misorientation angle between both grains up to 60°, we observed a GB structure which consists only of the square-typed units (see Fig. S1(c) in the SM [66]) similar to a GB with same macroscopic parameters in Al [69]. An alternative description of the Σ37c GB may be derived by considering it as a Σ3 GB with additional disconnections present to accommodate for the deviation of misorientation. The Σ37c deviates by $\Delta\theta = 60^\circ - 50.57^\circ = 9.43^\circ$ from the Σ3 GB. The Read–Shockley equation to derive the spacing of dislocations in low angle boundaries is $L = \frac{b}{2\sin(\theta/2)}$. If one applies it to this high-angle Σ37c GB, it turns out that the disconnection spacing L matches to the observed spacing of the trapezoidal units, assuming $b = a/6\langle 112\rangle = 0.3615\,\text{nm}/\sqrt{6} = 0.148\,\text{nm}$. Hence, the observed segregation of Ag into the trapezoidal units may be related to the regular arrangement of GB disconnection-type defects.

To conclude, the structural unit model is valid for this type of symmetric ⟨111⟩ tilt GB with misorientation angles between 46° and 60° [70]. Furthermore, the Σ37c ⟨111⟩ {347} GB could also be described by the Σ3 GB with additional disconnections, which are separated by a distance following the law for the formation of low angle GBs out of dislocations. When investigating a Σ37c ⟨111⟩ {347} GB in the Ag annealed Cu film [Fig. 2(c)], having the same misorientation of $(50.9 \pm 0.3)^\circ$, the same GB structure can be observed as in the case without Ag: The GB consists of two alternating subunits, one double-square unit, and one trapezoidal. Neither faceting nor phase transitions can be observed for this specific high-angle GB upon Ag segregation as it was the case for other GBs in Cu [26,29]. However, EDS showed a clear enrichment of Ag at the GB (see Fig. S3 in the SM [66]). Meiners *et al.* investigated Zr segregation at Cu in a similar GB and observed an enrichment of Zr at asymmetric steps [28]. As visible in Fig. S3 in the SM [66], this does not seem to be the case for Ag. Having a closer look at the Ag segregated

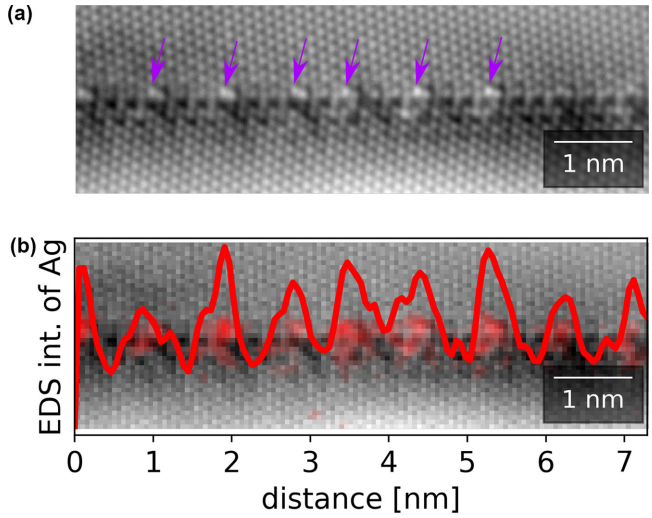

FIG. 3. (a) HAADF-STEM image at 120 kV of a Ag segregated Σ37c ⟨111⟩ {347} GB with a misorientation of $(50.6 \pm 0.3)^\circ$. (b) The intensity of the EDS signal of the Ag-Lα peak at 2.98 keV has maxima every ∼0.9 nm along the GB, coinciding with the trapezoidal units.

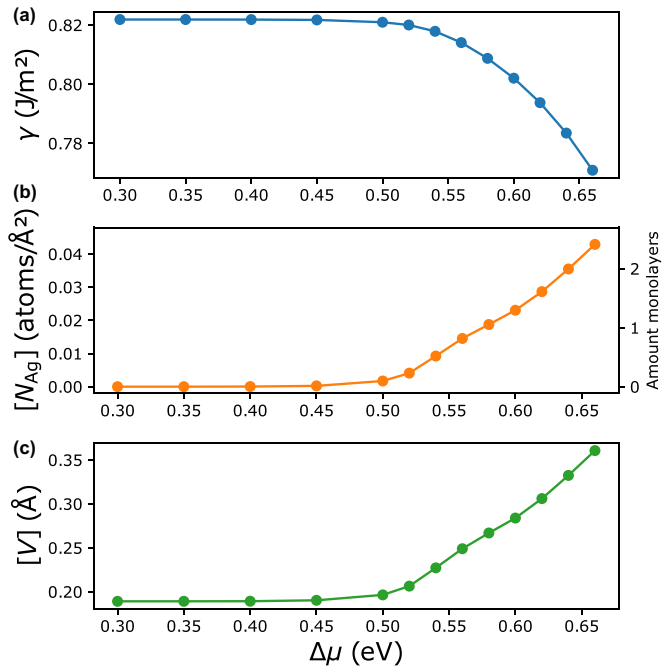

FIG. 4. Different thermodynamic properties for increasing chemical potential differences between Cu and Ag. Whereas (a) the free GB energy γ decreases, (b) the Ag excess $[N_{\mathrm{Ag}}]$, or equivalently the amount of monolayers covered by Ag atoms, and (c) excess volume $[V]$ of the GB increase with increasing chemical potential difference.

GB, the HAADF-STEM contrast of the atomic columns in the trapezoidal subunit seems to be increased [encircled in purple in Fig. 2(c)]. Thus, we decided to investigate the GB with Ag segregation by STEM but using a lower acceleration voltage. At 120 kV, the knock-on damage is reduced and less energy is transferred to the Ag atoms, avoiding a beam-induced change of their positions during acquisition and thus blurring of the atomic column contrast [71]. Indeed, a clearer picture can be drawn here [Fig. 3(a)]: One position within the trapezoidal subunit, from now on called "top position 1," has a significantly higher intensity (indicated by purple arrows). As the intensity in a HAADF-STEM image correlates with the atomic number of an element, this implies that Ag—which has a higher Z number (47) than Cu (29)—is enriched on that specific position. In a next step, near-atomic-resolution EDS was performed. The reduced acceleration voltage of 120 kV is also beneficial for STEM-EDS measurements due to an increased interaction cross-section for inelastic scattering, leading to a higher signal intensity [72]. It was not possible to achieve near atomic resolution in the STEM-EDS elemental maps acquired at 300 kV to resolve individual Ag columns within the GB structure as observed at 120 kV. Figure 3(b) shows the intensity of the Ag-Lα peak in the EDS dataset along the GB. Thereby, an integrated Ag line profile was obtained by measuring the Ag-Lα peak intensities along the GB with a width of 1.74 nm using hyperspy [73]. A significant increase in the Ag intensity can be observed at the trapezoidal unit. This supports the HAADF-STEM findings that the trapezoidal units are enriched in Ag.

C. MD/MC simulations and preferential Ag segregation sites

We also performed hybrid MD/MC simulations at 300 K with periodic boundary conditions on the same GB. The chemical potential difference between Ag and Cu was increased stepwise, acting as a driving force for Ag to segregate at the GB. In all simulations, as well as in the experiment, we only observed the zipper structure independent of the silver concentration. To investigate if GB phase transitions occur, we also performed MD/MC simulations with open boundaries at 900 K for 100 ns with different chemical potential differences [74]. We could once again only observe the zipper structure in the Σ37c ⟨111⟩ {347} GB.

We calculated the GB free energy as $\gamma = \gamma_0 - \int [N_{\mathrm{Ag}}] d\Delta\mu$, with γ_0 being the GB free energy without Ag excess [61]. The free energy of the GB decreases when the chemical potential difference increases [Fig. 4(a)], which signifies a stabilization of the GB upon Ag segregation. In contrast to that, the Ag excess $[N_{\mathrm{Ag}}]$ of the GB and thus the amount of monolayers occupied by Ag atoms increases [Fig. 4(b)]. To calculate the number of monolayers, the Ag excess was divided by the amount of atoms present in one {347} layer (containing only 3 atoms per CSL unit cell due to the high indices of the plane) divided by the area of the layer. The excess volume $[V]$ increases as well, as visible in Fig. 4(c). A major increase in excess volume is the main factor for embrittlement during Bi annealing [12–14]. In the Σ5 [001] (310) Cu GB, the excess volume tripled upon Bi segregation [75]. In our case, the GB's excess volume only doubled, which may help to explain why Ag segregation does not cause embrittlement [47]. It should be noted that other factors, like the local changes in atomic bonding of the GB or kinematic propagation of the crack tip along the GB, also contribute to the embrittlement of an alloy.

As in the experiment, we can observe that Ag substitutes specific GB sites on the atomic level. However, in atomistic

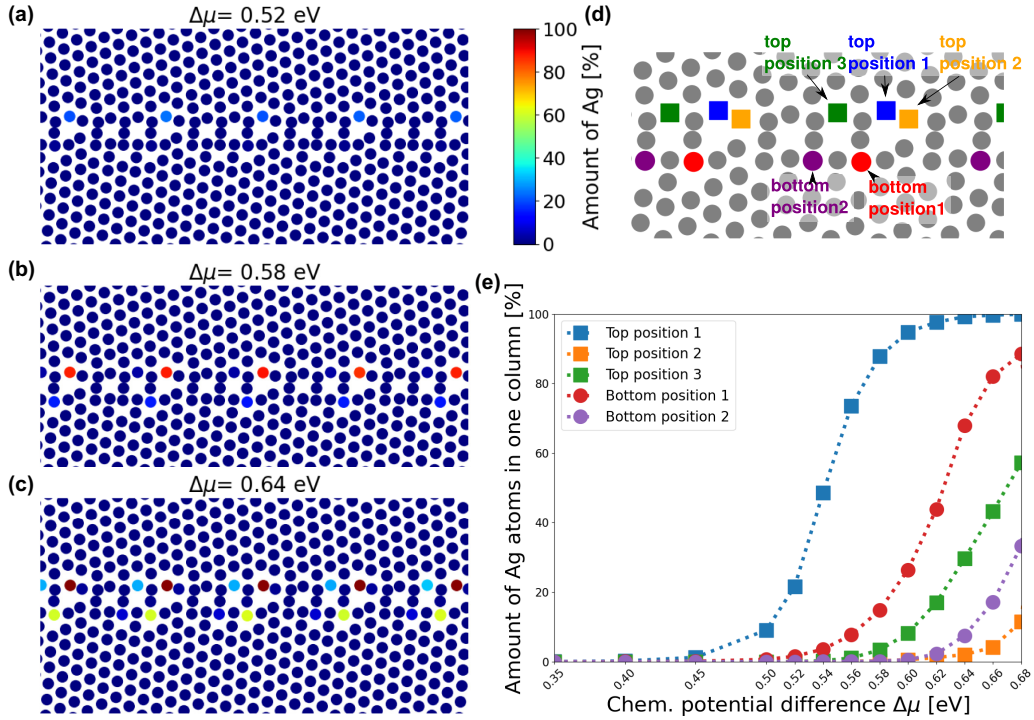

FIG. 5. Heat maps of the amount of Ag in each of the atomic columns at 300K are shown for different chemical potential differences: (a) 0.52 eV, (b) 0.58 eV, and (c) 0.64 eV. (d) Schematic showing the five positions within the GB structure to which Ag segregates predominantly. (e) The fraction of Ag atoms in each column as labeled in panel (d) increases with a higher chemical potential difference.

simulations we are even able to directly quantify the amount of Ag atoms in each atomic column. In Figs. 5(a)–5(c), the percentage of Ag atoms in each atomic column in the MD/MC simulations is plotted for three different chemical potentials. Even when the Ag concentration in the GB increases, the GB structure remains unchanged, with Ag just segregating to new substitutional sites within the structure. At a small chemical potential difference of 0.52 eV [Fig. 5(a)], the top position 1 is the only one which is occupied by Ag atoms with an amount of ∼22% of Ag out of all atoms in this column. Increasing the chemical potential difference to 0.58 eV [Fig. 5(b)], the top position 1 consists already of 88% Ag atoms and the bottom position 1 of ∼15% Ag atoms. Increasing the difference further to 0.64 eV [Fig. 5(c)], the top position 1 is completely occupied by Ag atoms (99%), while the bottom position 1 is occupied by ∼68% Ag atoms, followed by top position 3 (30% Ag atoms), bottom position 2 (8% Ag atoms), and top position 2 (2% Ag atoms). In Fig. 5(e), the amount of Ag at these five specific positions within the GB structure is plotted over the chemical potential difference. These five positions are the five with the highest Ag concentrations. First, the top position 1 is getting nearly completely filled, followed by bottom position 1. Then, top position 3, bottom position 1 and bottom position 2 get filled upon a higher chemical potential difference. At chemical potentials higher than 0.68 eV, the regular GB structure starts to collapse and Ag precipitates form. We repeated this analysis with datasets equilibrated at elevated temperatures (500 K instead of 300 K, see Fig. S4 in the SM [66]). They follow the same trend at slightly lower chemical potential differences.

The experimental determination of local solute concentrations within a GB structure is to date extremely challenging, but is important for connecting atomistic characteristics of GBs with their thermodynamic ensemble properties. Here, we use the obtained data from atomistic modeling under well defined boundary conditions as a baseline to quantify the atomic scale experimental observations. Two different approaches were used to find the best match for our experiment out of the modeled datasets with varying chemical potential differences. In a first approach, we use the Gibbsian interfacial excess (GIE) obtained from STEM-EDS as an averaged compositional quantity and in a second procedure we quantify the atomic column intensity in the HAADF-STEM images, comparing it to HAADF-STEM image simulations of the modeled datasets with different chemical potential differences. Both methods are explained in detail in the Appendix.

In the first approach, the concentration gradient of Ag is determined by STEM-EDS and averaged across several nanometers (here ∼7 nm) of the GB. Then, the concentration of Ag in both grains is subtracted from the concentration gradient, since we are only interested in the Ag excess at the GB. In a next step, the concentration is converted to an atomic density and then integrated to obtain the cumulative GIE, being $1.67 \pm 0.5\ \mathrm{nm}^{-2}$. It can then be compared to the ones from simulations with different amounts of Ag segregation, which were analyzed in the same way. Simulations with chemical potential differences of 0.55 to 0.59 eV have a GIE lying in the uncertainty range of the experimental observations. For lower chemical potential differences, less Ag segregates to the GB and thus the GIE would be lower. Is the chemical potential difference higher than 0.59 eV, more Ag

is present at the GB and thus the GIE is higher compared to the experimentally obtained value. It needs to be mentioned that the method is limited due to channelling effects since the analysis was performed when the sample was in zone axis, which might change concentration values. Also sample thickness and background noise can have an influence on concentration calculations.

In the second approach, the atomic column intensity of the Ag columns at the GB in the HAADF-STEM images is determined and related to the atomistic simulation by STEM image simulations. After subtracting a polynomial background from the atomic-resolution image, we normalized the intensities of the Ag columns to the averaged intensity of the Cu atomic columns within a grain to obtain comparable values. The experimental datasets reveal intensities of Ag within the top position 1 varying between 1.06 and 1.42 relative to the intensity of Cu atoms within the grain [see Appendix, Fig. 8(c)]. These values are then compared to HAADF-STEM image simulations of the atomistic models with different chemical potentials. The conditions for the HAADF-STEM image simulation have to be as close as possible to the real experimental conditions, including probe size, collection angles and sample thickness. For chemical potential differences of more than 0.56 eV, the intensity of Ag columns compared to Cu columns within the grains, is close to the experimentally observed value. At higher chemical potential differences than 0.58 eV, the intensity of the top position 1 does not change significantly since at this point, the column is already completely filled by Ag. However, at higher chemical potential differences, other columns get occupied with Ag and thus the intensities of these columns would increase. Apart from one column (see discussion below), this is not the case in our experiment. Thus, simulations with chemical potential differences higher than 0.6 eV would not match to our experiment.

To conclude, both methods for comparing simulation and experiment reveal that simulations with chemical potential differences between 0.55 to 0.59 eV would fit best to our experimental observations.

In Fig. 3(a), one can also observe that different columns of the top position 1 have different HAADF intensities. These values are normalized intensities relative to the average intensity of atomic columns within the grains. Knock-on damage, which can promote the redistribution of atoms and thus lead to variations in intensities during longer acquisition times, has been minimized by acquiring the data at 120 kV. Other factors, such as contamination, build-up, or sputtering of atoms at the GB can also lead to errors in the calculation of atomic column intensities. However, the intensity changes observed varying on a column-by-column basis over a length of about 7 nm can be as well related to local changes in Ag concentration. Furthermore, one bottom position 1 is visibly brighter. It is indicated in the Appendix [Fig. 8(c)] in the center of the image and has a value of 1.24. This value is substantially higher than the values of neighboring bottom positions 1, which have an intensity of 0.96, which correlates to a brightness intensity of a Ag-free column. This indicates that only at that specific position, the Ag intensity might be increased, indicating that the bottom position 1 is also partially filled by Ag. Furthermore, this observation underlines that local intensity changes might be present.

In the next section, we will elucidate the reason for Ag occupying these specific positions.

D. Influence of GB structure on preferential segregation sites

In the simulation, we observed a step-by-step filling of different atomic sites in the GB when increasing the chemical potential difference. We could correlate two of the states with our experimental observations, in which one atomic site (called top position 1) is filled nearly completely and a second atomic site (bottom position 1) is only partially filled. In the experiment, we can further observe site-by-site intensity variations in the HAADF intensity, which might be correlated to local changes in Ag occupancy of each atomic column. To understand the preferential site occupation of Ag atoms in the GB structure, we investigated different parameters such as the atomic volumes, distances to nearest neighbor atoms, Steinhardt parameters [76], and segregation energies of the different positions.

To this end, we first calculated the segregation energy of each position, defined as the energy difference of a system with Ag atoms on a GB site compared to a system with Ag atoms in the bulk [Fig. 6(a)] [21]. For this, we replaced the complete column of each segregation site in the GB individually with Ag [solid bars in Fig. 6(a)] and we could observe a negative segregation energy for all positions. We also tested segregation energies for implanting isolated Ag atoms to the investigated positions, but only small segregation energy differences compared to a completely filled column could be observed (Figs. S5 and S6 in the SM [66]). As expected, the top position 1, which gets occupied by Ag atoms first in the simulation and is also occupied by Ag in the experiment, is the one with the lowest segregation energy, followed by the bottom position 1. Interestingly, it seems that the top position 2 should be the third column being filled up based on the segregation energies, but it is the fifth and last column where Ag segregates to. The hatched bars in Fig. 6(a) show the segregation energies for successive filling of the columns as it was observed in the simulation, i.e., the segregation energy of bottom position 1 is calculated for a sample system with filled top position 1 and so on. For top position 2, the segregation energy for Ag atoms at this position was calculated in a system in which the other four columns were already occupied. Under these circumstances, the segregation energies are consistent with the results in Fig. 5.

As a different possible parameter for predicting preferential segregation sites, we investigated the free volume of each position in the GB structure using a Voronoi analysis [77]. Findings for the $\Sigma5$ $\langle 111 \rangle$ GB in Cu [12,78] or $\langle 110 \rangle$ GBs in Ni with Pd segregation [79] suggest that for bigger solute elements, the position in the GB structure with the highest volume would be the preferential segregation site. With the EAM potential, we found an excess Voronoi volume of 0.99 $Å^3$ for a substitutional Ag point defect, indicating that Ag atoms are clearly larger than Cu atoms and might prefer segregation sites with high free volume. In the investigated GB structure, the positions with the highest atomic volume in a pure Cu structure are top position 1 with 13.72 $Å^3$ and bottom position 1 with 13.79 $Å^3$, followed by top position 2 with 13.21 $Å^3$ [Fig. 6(b), gray bars]. The bigger atomic volume of top and

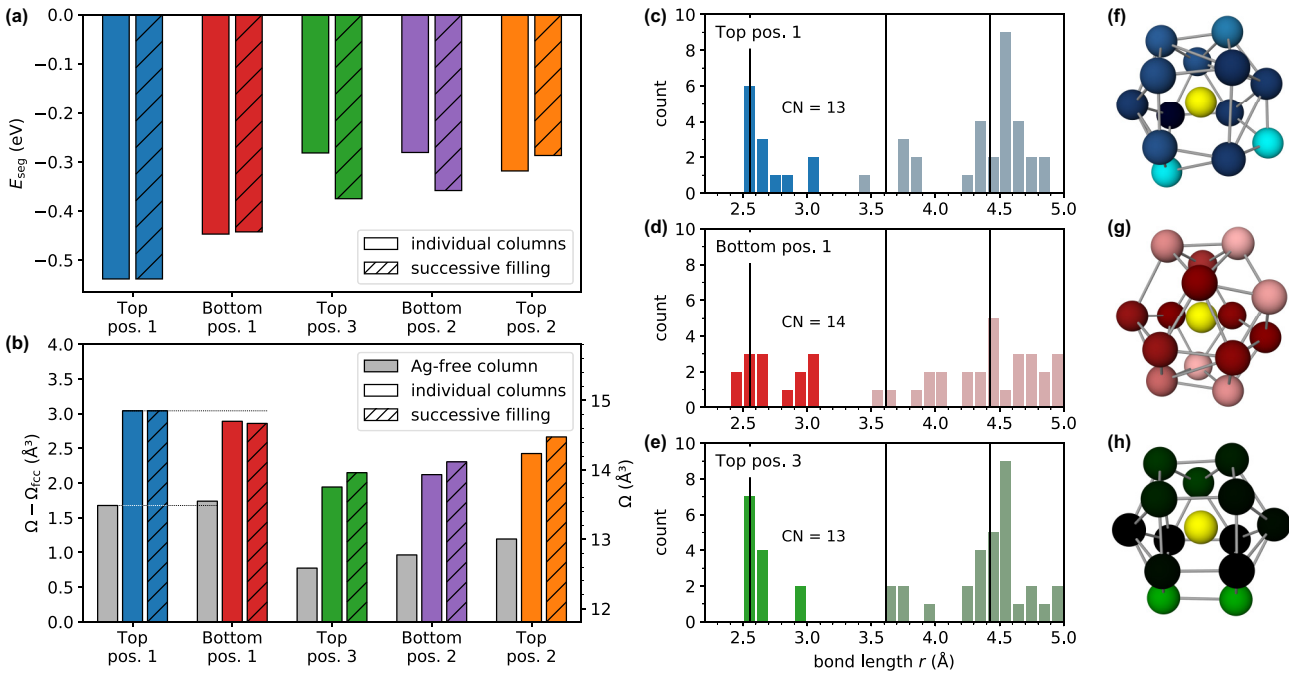

FIG. 6. Properties of different GB sites. (a) The Ag segregation energy at each position. The solid bars represent individual segregation energies and the hatched bars represent segregation energies when successively filling the positions (e.g., the hatched green bar shows the segregation energy when top position 1 and bottom position 1 are already filled). (b) Local Voronoi excess volumes (atomic volume Ω for each column minus the atomic volume of fcc atoms Ω_{fcc}). The absolute volume is shown on the right axis. For the Ag-free system (gray bars), bottom position 1 has a slightly higher volume compared to top position 1 ($\Delta\Omega = 0.06$ Å^3). Top position 1, however, expands to a higher atomic volume ($\Delta\Omega = -0.15$ Å^3) upon insertion of Ag than bottom position 1 (colored bars). (c–e) Diagrams showing the radial distances and amount of next atoms for the first three positions getting occupied. The radial distances are measured in pure Cu GBs. The black lines indicate the neighbor distances in defect-free fcc. Darker bars show bonds shorter than 3.25 Å, which corresponds roughly to the first neighbor shell. The corresponding coordination numbers (CN) are also shown. (f–h) First neighbor shell of an atom (yellow) in top position 1 (f), bottom position 1 (g), and top position 3 (h). The brightness indicates the bond length of the neighbor atom (dark being 2.55 Å and light being 3.10 Å).

bottom position 1 compared to the rest of the sites can explain the preferential segregation to these two sites. Even though their atomic volumes are similar to each other, the top position 1 is occupied by Ag atoms prior to bottom position 1.

Differences in atomic strain at different sites can also be a factor for preferential site occupation [36,80]. Thus, we investigated the volume expansion of all five segregation sites upon Ag filling of each site individually [filled colored bars in Fig. 6(b)] or upon successive filling (hatched bars) following the order shown in Fig. 5(e). We can observe that top position 1 has a slightly larger volume than bottom position 1 after being filled with Ag, even though there was a small tendency in the opposite direction in the pure Cu case (bottom position 1 was slightly larger compared to top position 1). This is true regardless of whether top position 1 was already filled by a Ag atom (hatched bar) or only bottom position 1 (colored bar) is occupied by Ag. It indicates that top position 1 can expand more easily compared to bottom position 1, which can lead to a preferential position. However, looking at the atomic volumes of the consecutive positions, the expected trend of decreasing atomic volumes for less favorable positions cannot be observed. According to the atomic volumes, top position 2 should be the position being occupied after top and bottom position 1. However, it is top position 3, with the lowest atomic volume both in a pure Cu cell and when it is occupied by Ag. Thus, the atomic volume alone is insufficient to explain the preferential segregation sites.

In a next step, we also had a look at the specific atomic environments of different positions. Therefore, we investigated the bond length of all neighboring atoms as shown in Figs. 6(c)–6(h) for the first three positions. In Figs. 6(c)–6(e) it is shown that the closest atoms are present in bond distances between 2.4/2.5 Å to 3.1 Å. In none of the three investigated positions, atoms occur with bond distances of 3.1 to 3.4 Å, but only again at higher distances than 3.4 Å. In a bulk Cu lattice, the nearest neighbor atoms have a distance of 2.55 Å (indicated by a black line). In bottom position 1, two atoms are even slightly closer than that. This might be unfavorable for Ag due to its atomic size mismatch, but due to the delocalized nature of the metallic bond it is difficult to draw definite conclusions from the first neighbor shell environment alone. All in all, no striking, qualitative differences between the three diagrams are visible that could serve as a simple predictor for preferential segregation sites.

Furthermore, Scheiber *et al.* found a linear correlation between the fifth Steinhardt order parameter [76] and the segregation energy [81]. We therefore also tried this analysis (Fig. S7 in the SM [66], calculated using the software pyscal [82]), but could find no such correlation for any of the first 12 parameters. This suggests that the changes in the bonding

environment are relatively delocalized in our case so that they are not easily detectable with methods that consider only the next-neighbor environment. Therefore, the bond lengths and number of nearest neighbor atoms or the shape of the polyhedron are not suitable as simple predictors to determine preferred segregation sites within a GB in a metallic system in accordance with the observations of Ziebarth *et al.* for Fe impurities in Si GBs [83].

Furthermore, preferential sites of solutes were also identified due to dangling bonds or changes of covalent bonds especially in ceramic materials or semimetals [84–87]. Upon changes in the electronic structure, the cohesive energy also changes and can thus lead to embrittlement. Pronounced effects can be observed if the solute atoms differ in electronegativity compared to the host element [88,89]. However, for Ag in Cu, both elements have similar electronegativity and embrittlement of Cu due to Ag segregation has not been observed. Since both are metals, no dangling or covalent bonds are expected and changes in the electronic band structure are not accessible with the methods used in the present work.

We can conclude that besides the segregation energy, no simple predictor of the preferential segregation sites could be found. While local free volume plays a role, local bonding effects and interactions between segregant atoms cannot be neglected and depend on the complex atomic environment of the GB. However, these are not easy to compute and thus not suitable for simple predictions.

IV. CONCLUSION

We investigated the segregation behavior of Ag in a symmetric tilt GB in Cu and different parameters which might affect the site occupation combining experimental observations and atomistic simulations. The atomic structure of a $\Sigma 37c$ $\langle 111 \rangle$ $\{347\}$ GB in copper was resolved using HAADF-STEM. The same structure was replicated in MD simulations. After Ag alloying, Ag atoms only substitute specific positions in the GB. Neither faceting nor phase transition was observed. Comparing experiment and hybrid MD/MC simulations using HAADF-STEM intensity changes and Gibbsian interfacial excess determination, we conclude that simulations with a Ag excess of 0.015 atoms $Å^{-2}$ to 0.019 atoms $Å^{-2}$ match best to our experiment (equivalent to a chemical potential difference of $\Delta\mu = 0.56$ meV to 0.58 meV at 300 K). In these cases, two columns in the GB structure are occupied with Ag, whereas top position 1 is mostly filled and bottom position 1 only partially. In the experiment, local changes of Ag occupation between columns are observed, which can induce site-specific changes in GB properties. We investigated the relevance of different parameters (volume, configuration of surrounding atoms, Steinhardt order parameter) for predicting preferential segregation sites in the GB structure. The preferential segregation sites are not solely determined by the local volume of each site and its expansion upon segregation. Also the bond lengths of surrounding atoms and the Steinhardt order parameters do not show a simple clear trend for the order in which the positions are filled up according to simulations. Only the calculation of the segregation energy, which takes into account the local atomic bonding in each position, follows the same trend as the occupation of Ag in specific sites. A combination of both experiment and simulation as presented above is needed to determine the atomic level distribution of solutes at GBs and for understanding the atomistic origin of GB segregation. These two ingredients ultimately provide the link to the thermodynamic characteristics of the interface and how they affect macroscopic material properties.

The main datasets of this study are published in Ref. [55].

ACKNOWLEDGMENTS

We gratefully acknowledge G. Richter's team from the Max Planck Institute for Intelligent Systems for producing the Cu thin film and T. Oellers for the Ag deposition at the Ruhr-Universität Bochum. The authors thank N. Peter for helpful discussions and initiating this project by assisting in Ag deposition on the film. This project has received funding from the European Research Council (ERC) under the European Union's Horizon 2020 research and innovation programme (Grant Agreement No. 787446; GB-CORRELATE).

L.L. performed the experimental sample preparation, HAADF-STEM investigations, and analysis of the obtained datasets. C.H.L. and G.D. designed the concept of the experimental study. T.B. performed the simulations and analyses of the simulation data. G.R. provided the Cu thin film, the main material used in this study. The project was supervised by C.H.L. and G.D., who also contributed to discussions. G.D. secured funding for L.L. and T.B. via the ERC grant GB-CORRELATE. L.L. and T.B. prepared the initial draft and all authors contributed to the preparation of the final manuscript.

APPENDIX: COMPARISON OF EXPERIMENT AND SIMULATION TO QUANTIFY THE AG EXCESS

We used two methods to determine the local Ag excess at the GB by comparing experiment with atomistic simulations. In the first method, we determine the Gibbsian interfacial excess (GIE) from the STEM-EDS and compared it to the GIE obtained from MD/MC simulations. In the second method, we measure the atomic column intensity in HAADF-STEM images of the top position 1 in the GB relative to the bulk Cu columns and compared it to HAADF-STEM image simulations using the MD/MC cells as input.

Method 1: Determining the Gibbsian interfacial excess from STEM-EDS

We determine the GIE from STEM-EDS datasets similar to the procedure described in Refs. [90,91]. We used the EDS maps acquired at 120 kV to reduce knock-on damage and to maximize the x-ray yield. In a first step, the Ag content was quantified using the Velox Software (version 3.5). For the quantification, a standard-less Cliff–Lorimer quantification with absorption correction was used, which takes into account the actual geometry of the detectors and the stage tilt. The sample thickness was set to 50 nm and a Brown–Powell ionization cross-section model was used. In a second step, the Ag concentration profile across a GB with a width of 7 nm parallel to the GB plane—equivalent to about 7 structural units of the $\Sigma 37c$ $\langle 111 \rangle$ $\{347\}$ GB—was summed. Such a

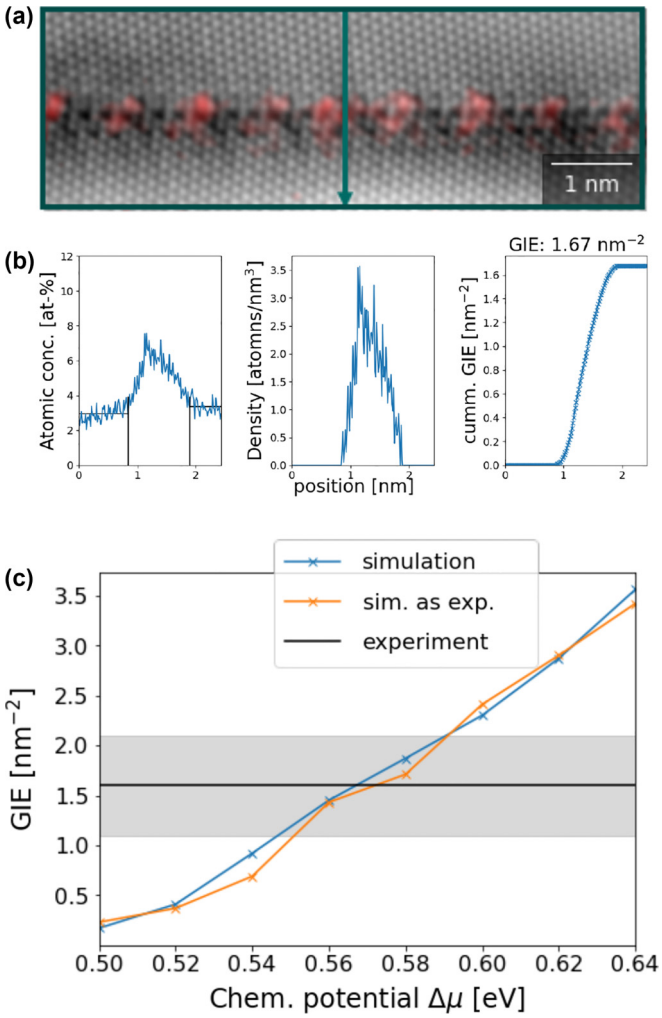

FIG. 7. Comparing the calculated GIE value of simulations with the experiment. (a) HAADF-STEM image with EDS signal of Ag overlaid. The concentration profile of Ag was measured along the arrow, with a width equal to the frame size. (b) Diagrams showing the steps needed to convert the concentration to the GIE. (c) Comparison of the GIE of simulations with experiments. All simulation datasets for the different chemical potentials were equilibrated at 300 K.

concentration profile is shown in Fig. 7(b) on the left side. Since we are only interested in the Ag excess at the GB, thus the surplus of Ag content, we subtracted the Ag concentration in the grains. To access the GIE, the Ag concentration needs to be converted to an atomic density. Therefore, the density of fcc Cu along the ⟨111⟩ direction was used, being 84.67 atoms/nm^2 for a lattice parameter of $a = 3.615$ Å. This is shown in Fig. 7(b) in the middle. The integral of the atomic density is then equal to the GIE [Fig. 7(b), right side]. An experimental value of the GIE of about 1.67 ± 0.5 nm^{-2} was experimentally determined for 2 independent EDS data sets acquired at different GB positions.

For estimating the errors present in our calculation, the averaged Cu density as well as the integration width were changed. Thereby, changing the atomic density by 6% can lead to an uncertainty in the GIE of up to 22%. A decrease of 30% of the integration width can lead to a decrease in GIE of 15 %. Furthermore, the quantification of Ag concentration by EDS has an uncertainty of ±2 at-%. To conclude, the method presented above is sensitive to many parameters affecting its accuracy to determine the GIE. Thus, we used the experimentally measured GIE only as a rough guideline to evaluate which range of simulated Ag excess values and hence chemical potential difference match to the experiment. Therefore, we performed the same analysis as described above for the simulated datasets, even though the GIE could be extracted from the simulated datasets in a direct manner as shown in Fig. 4(b). We compared the directly obtained GIE for Ag in the simulated datasets with the ones calculated analogous to the experiment and observed deviations of max. 5%. This shows that the pathway of obtaining the GIE is fairly correct and only experimental uncertainties (like the absolute quantification of Ag and defining the integration width of the Ag peak) can affect the experimentally extracted GIE. As expected, with increase of a chemical potential difference, the GIE increases since more Ag diffuses into the system and also more Ag is present at the GB. The simulations overlap with the experiments for chemical potential differences between 0.55 and 0.59 eV.

Method 2: Quantifying the intensity of Ag columns from atomic resolution using the HAADF-STEM images

To estimate the amount of Ag in atomic columns within the GB, we quantify the atomic column contrast in the HAADF-STEM images. Due to the complex atomic arrangements of atoms at the GB core, we determine the intensity of the Ag-rich columns relative to atomic columns within the grain as a reference. The experimental datasets are then compared to HAADF-STEM image simulations using the MD/MC simulation cells as input. In a first step, a 2D-polynomial background subtraction was performed on the experimental images [Fig. 8(a)]. Then, a peak finding algorithm of the Python package ATOMAP (version 0.3.1) was used to determine the position of each of the atomic columns and their single peak intensity values [92]. The intensity values got normalized by the average of the intensity of atomic columns located in both grains [see Fig. 8(b)]. In a final step, the intensity of the top position 1 within the GB structure was extracted. The intensities in the experimental image vary between 1.06 and 1.39, excluding the minimum and maximum since they might stem from nonaccurate background substraction. Thus, in average, the top position 1 has an intensity of 1.18 ± 0.15 as shown in Fig. 8(c). Besides one bottom position 1, which has an intensity value of 1.24, the intensity of all other positions does not show a substantial increase from the averaged value of 1 and are thus not listed here. This method also exhibits several uncertainties, as the intensity value might be influenced in the first place by the sample thickness, amorphous layers on the surface of the sample, or oxides and background noise, and in the second step by using different background correction methods or extracting the intensity of the atomic columns with

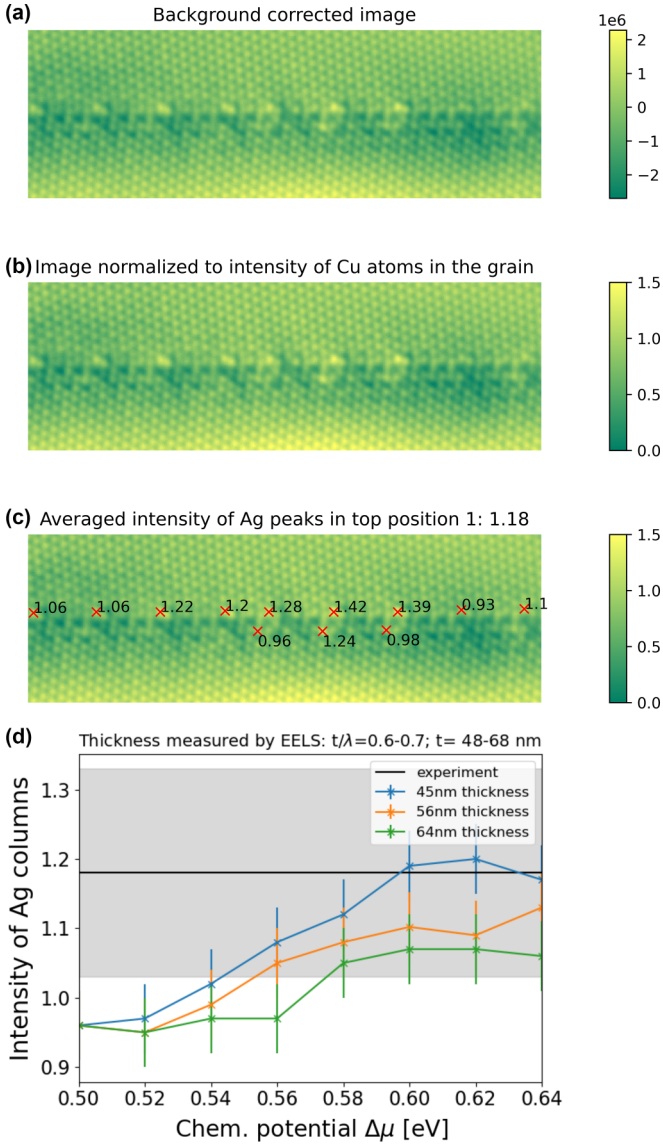

FIG. 8. Comparing the HAADF-STEM intensities of atomic columns enriched with Ag with the HAADF-STEM intensity of Cu columns in the grain. (a) Intensity of a background corrected HAADF-STEM image. (b) The intensity values of all columns were measured and normalized by the average intensity values of atomic columns in the grains. (c) Intensity values of the Ag enriched columns. (d) A comparison was performed for the experimental image with HAADF-STEM image simulations, using the same imaging conditions as used in the experiment. A thickness range for the simulation cells was used to take into account uncertainties for the experimentally determined thickness value of the sample.

other algorithms. Thus, great care has to be taken and the final results can be only understood as a rough estimation.

For the comparison with MD/MC simulations, a simulation cell of a similar thickness as the lamella in the experiment is needed. We estimated the thickness of the investigated sample to be between 55 and 64 nm using EELS and the thickness determination according to Malis *et al.* [93]. In a next step, we took the MD/MC cells and replicated them periodically along the ⟨111⟩ direction to the desired thickness. In a next step, we used these cells to create synthetic HAADF-STEM images using the multislice algorithm with parameters which match the experimental parameters as well as possible (an aberration-free electron probe with 120 kV, semiangle of 24 mrad, focal spread of 60 Å, an annular detector detecting with a collection angle range of 95 to 200 mrad, corresponding to the setting of our HAADF detector in the experiment, and a beam scan step size of 0.14 Å, which corresponds to the pixel size). The image simulation was performed with the Python library abTEM version 1.0.0b11 [94].

Having the simulated HAADF-STEM images for each chemical potential, we followed the same steps as for the experimental images. Only the first step of background correction was not necessary since the contribution from the background is negligible in the simulation. All atomic column positions and their peak intensities were determined using ATOMAP. The intensity of all columns was normalized by the average intensity of the atomic columns within the bulk grains. In Fig. 8(d), the change in intensity ratio of the top position 1 in dependence of chemical potential difference is shown for different simulation cell thicknesses. The average intensity ratio determined from the experiment is given as black line and the gray shaded area represents the uncertainty range considering different columns. The intensity values of top position 1 from the simulated images start to overlap with the ones from experiments for chemical potential differences at about 0.56 to 0.58 eV, depending on the simulated thickness. When increasing the chemical potential difference further, we can see that other positions (as bottom position 1, 2 and top position 2, 3), get occupied by Ag and thus increase in intensity values. In the experiment, the HAADF STEM intensities of top position 2, 3 and bottom position 1, 2 do not show significantly higher values than other positions within the GB [besides bottom position 1 in one position as indicated in Fig. 8(c)]. For simulated datasets with a chemical potential difference of more than 0.60 eV, a significant increase in HAADF-STEM intensity in other atomic columns is detected. Thus, when comparing HAADF-STEM intensities of simulations and experiment, simulations using a chemical potential difference between 0.56 and 0.60 eV are matching best with the experiments.

To conclude, both independent methods predict that a chemical potential difference between 0.56 and 0.60 eV would fit best to our experimental dataset.

[1] S. Özerinç, K. Tai, N. Q. Vo, P. Bellon, R. S. Averback, and W. P. King, Grain boundary doping strengthens nanocrystalline copper alloys, Scr. Mater. **67**, 720 (2012).

[2] R. K. Koju and Y. Mishin, Atomistic study of grain-boundary segregation and grain-boundary diffusion in Al-Mg alloys, Acta Mater. **201**, 596 (2020).

[3] I. Basu, K. G. Pradeep, C. Mießen, L. A. Barrales-Mora, and T. Al-Samman, The role of atomic scale segregation in designing highly ductile magnesium alloys, Acta Mater. **116**, 77 (2016).

[4] D. Y. Khang, H. Jiang, Y. Huang, and J. A. Rogers, A stretchable form of single-crystal silicon for high-performance electronics on rubber substrates, Science **311**, 208 (2006).

[5] J. Schäfer and K. Albe, Influence of solutes on the competition between mesoscopic grain boundary sliding and coupled grain boundary motion, Scr. Mater. **66**, 315 (2012).

[6] T. J. Rupert, J. C. Trenkle, and C. A. Schuh, Enhanced solid solution effects on the strength of nanocrystalline alloys, Acta Mater. **59**, 1619 (2011).

[7] N. Q. Vo, J. Schäfer, R. S. Averback, K. Albe, Y. Ashkenazy, and P. Bellon, Reaching theoretical strengths in nanocrystalline Cu by grain boundary doping, Scr. Mater. **65**, 660 (2011).

[8] W. Wei and H. J. Grabke, The effect of alloying elements on the grain boundary segregation of phosphorus in iron and the intergranular corrosion of the Fe-P system, Corros. Sci. **26**, 223 (1986).

[9] M. P. Seah, Adsorption-induced interface decohesion, Acta Metall. **28**, 955 (1980).

[10] P. Lejček, *Grain Boundary Segregation in Metals*, Vol. 136 (Springer, Berlin, 2010).

[11] W. Hampe, Beiträge zu der Metallurgie des Kupfers, Zeitschrift für das Berg-, Hütten- und Salinenwesen im Deutschen Reich **22**, 93 (1874).

[12] G. Duscher, M. F. Chisholm, U. Alber, and M. Rühle, Bismuth-induced embrittlement of copper grain boundaries, Nat. Mater. **3**, 621 (2004).

[13] V. J. Keast, J. Bruley, P. Rez, J. M. Maclaren, and D. B. Williams, Chemistry and bonding changes associated with the segregation of bi to grain boundaries in Cu, Acta Mater. **46**, 481 (1998).

[14] R. Schweinfest, A. T. Paxton, and M. W. Finnis, Bismuth embrittlement of copper is an atomic size effect, Nature **432**, 1008 (2004).

[15] N. G. Ainslie, R. E. Hoffman, and A. U. Seybolt, Sulfur segregation at α-iron grain boundaries–I, Acta Metall. **8**, 523 (1960).

[16] W. R. Thomas and B. Chalmers, The segregation of impurities to grain boundaries, Acta Metall. **3**, 17 (1955).

[17] G. H. Li and L. D. Zhang, Relationship between misorientation and bismuth induced embrittlement of [001] tilt boundary in copper bicrystal, Scr. Metall. Mater. **32**, 1335 (1995).

[18] B. D. Powell and H. Mykura, The segregation of bismuth to grain boundaries in copper-bismuth alloys, Acta Metall. **21**, 1151 (1973).

[19] E. D. Hondros, Grain boundary segregation: The current situation and future requirements, J. Phys. Colloques **36**, C4-117 (1975).

[20] T. Watanabe, Structural effects on grain boundary segregation, hardening, and fracture, J. Phys. Colloques **46**, C4-555 (1985).

[21] V. Vitek and G. J. Wang, Atomic structure of grain boundaries and intergranular segregation, J. Phys. **43**, 147 (1982).

[22] P. Wynblatt and D. Chatain, Anisotropy of segregation at grain boundaries and surfaces, Metall. Mater. Trans. A **37**, 2595 (2006).

[23] P. Lejček, M. Všianská, and M. Šob, Recent trends and open questions in grain boundary segregation, J. Mater. Res. **33**, 2647 (2018).

[24] D. Raabe, M. Herbig, S. Sandlöbes, Y. Li, D. Tytko, M. Kuzmina, D. Ponge, and P. P. Choi, Grain boundary segregation engineering in metallic alloys: A pathway to the design of interfaces, Curr. Opin. Solid State Mater. Sci. **18**, 253 (2014).

[25] P. R. Cantwell, T. Frolov, T. J. Rupert, A. R. Krause, C. J. Marvel, G. S. Rohrer, J. M. Rickman, and M. P. Harmer, Grain boundary complexion transitions, Annu. Rev. Mater. Res. **50**, 465 (2020).

[26] T. Frolov, M. Asta, and Y. Mishin, Segregation-induced phase transformations in grain boundaries, Phys. Rev. B **92**, 020103(R) (2015).

[27] T. G. Ference and R. W. Balluffi, Observation of a reversible grain boundary faceting transition induced by changes of composition, Scr. Metall. **22**, 1929 (1988).

[28] T. Meiners, J. M. Duarte, G. Richter, G. Dehm, and C. H. Liebscher, Tantalum and zirconium induced structural transitions at complex [111] tilt grain boundaries in copper, Acta Mater. **190**, 93 (2020).

[29] N. J. Peter, T. Frolov, M. J. Duarte, R. Hadian, C. Ophus, C. Kirchlechner, C. H. Liebscher, and G. Dehm, Segregation-Induced Nanofaceting Transition at an Asymmetric Tilt Grain Boundary in Copper, Phys. Rev. Lett. **121**, 255502 (2018).

[30] N. J. Peter, M. J. Duarte, C. Kirchlechner, C. H. Liebscher, and G. Dehm, Faceting diagram for Ag segregation induced nanofaceting at an asymmetric Cu tilt grain boundary, Acta Mater. **214**, 116960 (2021).

[31] B. Feng, T. Yokoi, A. Kumamoto, M. Yoshiya, Y. Ikuhara, and N. Shibata, Atomically ordered solute segregation behaviour in an oxide grain boundary, Nat. Commun. **7**, 11079 (2016).

[32] S. Ma, P. R. Cantwell, T. J. Pennycook, N. Zhou, M. P. Oxley, D. N. Leonard, S. J. Pennycook, J. Luo, and M. P. Harmer, Grain boundary complexion transitions in WO_3- and CuO-doped TiO_2 bicrystals, Acta Mater. **61**, 1691 (2013).

[33] H. I. Yoon, D. K. Lee, H. B. Bae, G. Y. Jo, H. S. Chung, J. G. Kim, S. J. L. Kang, and S. Y. Chung, Probing dopant segregation in distinct cation sites at perovskite oxide polycrystal interfaces, Nat. Commun. **8**, 1417 (2017).

[34] C.-X. Li, S.-H. Dang, L.-P. Wang, C.-L. Zhang, and P.-D. Han, First principles investigation into effects of Cr on segregation of S or Cl at α-FeΣ5(210) grain boundary, Mater. Res. Innov. **18**, S4-1012 (2014).

[35] P. Parajuli, D. Romeu, V. Hounkpati, R. Mendoza-Cruz, J. Chen, M. J. Yacamán, J. Flowers, and A. Ponce, Misorientation dependence grain boundary complexions in symmetric tilt Al grain boundaries, Acta Mater. **181**, 216 (2019).

[36] J. F. Nie, Y. M. Zhu, J. Z. Liu, and X. Y. Fang, Periodic segregation of solute atoms in fully coherent twin boundaries, Science **340**, 957 (2013).

[37] D. McLean, *Grain Boundaries in Metals* (Clarendon Press, Oxford, UK, 1957), pp. 1–346.

[38] E. D. Hondros and M. P. Seah, The theory of grain boundary segregation in terms of surface adsorption analogues, Metall. Trans. A **8**, 1363 (1977).

[39] R. H. Fowler, *Statistical Thermodynamics* (Cambridge University Press Archive, Cambridge, UK, 1939).

[40] C. L. White and W. A. Coghlan, The spectrum of binding energies approach to grain boundary segregation, Metall. Trans. A **8**, 1403 (1977).

[41] C. L. White and D. F. Stein, Sulfur segregation to grain boundaries in Ni_3Al and $Ni_3(Al, Ti)$ alloys, Metall. Mater. Trans. A **9**, 13 (1978).

[42] D. Udler and D. N. Seidman, Solute segregation at [001] tilt boundaries in dilute fcc alloys, Acta Mater. **46**, 1221 (1998).

[43] M. Wagih and C. A. Schuh, Grain boundary segregation beyond the dilute limit: Separating the two contributions of site spectrality and solute interactions, Acta Mater. **199**, 63 (2020).

[44] L. Huber, R. Hadian, B. Grabowski, and J. Neugebauer, A machine learning approach to model solute grain boundary segregation, npj Comput. Mater. **4**, 64 (2018).
[45] F. Debray and P. Frings, State of the art and developments of high field magnets at the "laboratoire national des champs magnétiques intenses," C. R. Phys. **14**, 2 (2013).
[46] S. Zherlitsyn, B. Wustmann, T. Herrmannsdorfer, and J. Wosnitza, Status of the pulsed-magnet-development program at the dresden high magnetic field laboratory, IEEE Trans. Appl. Supercond. **22**, 4300603 (2012).
[47] A. Y. Lozovoi, A. T. Paxton, and M. W. Finnis, Structural and chemical embrittlement of grain boundaries by impurities: A general theory and first-principles calculations for copper, Phys. Rev. B **74**, 155416 (2006).
[48] Y. Sakai, K. Inoue, T. Asano, H. Wada, and H. Maeda, Development of high-strength, high-conductivity Cu–Ag alloys for high-field pulsed magnet use, Appl. Phys. Lett. **59**, 2965 (1991).
[49] Y. Sakai and H. J. Schneider-Muntau, Ultra-high strength, high conductivity Cu-Ag alloy wires, Acta Mater. **45**, 1017 (1997).
[50] H. Y. Yang, Z. C. Ma, C. H. Lei, L. Meng, Y. T. Fang, J. B. Liu, and H. T. Wang, High strength and high conductivity Cu alloys: A review, Sci. China Technol. Sci. **63**, 2505 (2020).
[51] S. V. Divinski, H. Edelhoff, and S. Prokofjev, Diffusion and segregation of silver in copper Σ5(310) grain boundary, Phys. Rev. B **85**, 144104 (2012).
[52] T. Frolov, S. V. Divinski, M. Asta, and Y. Mishin, Effect of Interface Phase Transformations on Diffusion and Segregation in High-Angle Grain Boundaries, Phys. Rev. Lett. **110**, 255502 (2013).
[53] R. K. Koju and Y. Mishin, Relationship between grain boundary segregation and grain boundary diffusion in Cu-Ag alloys, Phys. Rev. Mater. **4**, 073403 (2020).
[54] P. R. Subramanian and J. H. Perepezko, The Ag-Cu (silver-copper) system, J. Phase Equilib. **14**, 62 (1993).
[55] L. Langenohl, T. Brink, G. Richter, G. Dehm, and C. H. Liebscher, Dataset belonging to the paper "Atomic resolution observations of silver segregation in a [111] tilt grain boundary in copper" (Zenodo, 2022), https://doi.org/10.5281/zenodo.7646180.
[56] H. H. Jin, C. Shin, and J. Kwon, Fabrication of a TEM sample of ion-irradiated material using focused ion beam microprocessing and low-energy ar ion milling, J. Electron Microsc. **59**, 463 (2010).
[57] S. Plimpton, Fast parallel algorithms for short-range molecular dynamics, J. Comput. Phys. **117**, 1 (1995).
[58] A. P. Thompson, H. M. Aktulga, R. Berger, D. S. Bolintineanu, W. M. Brown, P. S. Crozier, P. J. in 't Veld, A. Kohlmeyer, S. G. Moore, T. D. Nguyen, R. Shan, M. J. Stevens, J. Tranchida, C. Trott, and S. J. Plimpton, LAMMPS—A flexible simulation tool for particle-based materials modeling at the atomic, meso, and continuum scales, Comput. Phys. Commun. **271**, 108171 (2022).
[59] P. L. Williams, Y. Mishin, and J. C. Hamilton, An embedded-atom potential for the Cu–Ag system, Modell. Simul. Mater. Sci. Eng. **14**, 817 (2006).
[60] B. Sadigh, P. Erhart, A. Stukowski, A. Caro, E. Martinez, and L. Zepeda-Ruiz, Scalable parallel Monte Carlo algorithm for atomistic simulations of precipitation in alloys, Phys. Rev. B **85**, 184203 (2012).
[61] T. Frolov and Y. Mishin, Thermodynamics of coherent interfaces under mechanical stresses. II. Application to atomistic simulation of grain boundaries, Phys. Rev. B **85**, 224107 (2012).
[62] T. Frolov and Y. Mishin, Thermodynamics of coherent interfaces under mechanical stresses. I. Theory, Phys. Rev. B **85**, 224106 (2012).
[63] A. Stukowski, Visualization and analysis of atomistic simulation data with OVITO—The Open Visualization Tool, Modell. Simul. Mater. Sci. Eng. **18**, 015012 (2010).
[64] G. Katz, The epitaxy of copper on sapphire, Appl. Phys. Lett. **12**, 161 (1968).
[65] G. Dehm, H. Edongué, T. Wagner, S. H. Oh, and E. Arzt, Obtaining different orientation relationships for Cu films grown on (0001) α-Al_2O_3 substrates by magnetron sputtering, Zeitschrift für Metallkunde **96**, 249 (2005).
[66] See Supplemental Material at http://link.aps.org/supplemental/10.1103/PhysRevB.107.134112 for additional experimental and simulation data.
[67] H. J. Frost, M. F. Ashby, and F. Spaepen, A catalogue of [100], [110], and [111] symmetric tilt boundaries in face-centered cubic hard sphere crystals, Tech. Rep. (Harvard Division of Applied Sciences, 1982), https://nrs.harvard.edu/urn-3HUL.InstRepos13851353.
[68] J. Han, V. Vitek, and D. J. Srolovitz, The grain-boundary structural unit model redux, Acta Mater. **133**, 186 (2017).
[69] S. Ahmad, T. Brink, C. H. Liebscher, and G. Dehm, Microstates and defects of incoherent Σ3 [111] twin boundaries in aluminum, Acta Mater. **243**, 118499 (2023).
[70] J. Han, S. L. Thomas, and D. J. Srolovitz, Grain-boundary kinetics: A unified approach, Prog. Mater. Sci. **98**, 386 (2018).
[71] R. F. Egerton, P. Li, and M. Malac, Radiation damage in the TEM and SEM, Micron **35**, 399 (2004).
[72] D. C. Bell and N. Erdmann, *Low Voltage Electron Microscopy: Principles and Applications*, 1st ed., Vol. 1 (Wiley, New York, NY, 2013).
[73] F. de la Peña, E. Prestat, V. T. Fauske, P. Burdet, J. Lähnemann, T. Furnival, P. Jokubauskas, M. Nord, T. Ostasevicius, K. E. MacArthur, D. N. Johnstone, M. Sarahan, T. Aarholt, J. Taillon, pquinn dls, V. Migunov, A. Eljarrat, J. Caron, T. Poon, S. Mazzucco, C. Francis, B. Martineau, actions user, S. Somnath, T. Slater, N. Tappy, M. Walls, N. Cautaerts, F. Winkler, and DENSmerijn, "hyperspy/hyperspy: Release v1.6.5" (2021), Zenodo, doi: 10.5281/ZENODO.5608741.
[74] T. Frolov, D. L. Olmsted, M. Asta, and Y. Mishin, Structural phase transformations in metallic grain boundaries, Nat. Commun. **4**, 1899 (2013).
[75] A. Y. Lozovoi and A. T. Paxton, Boron in copper: A perfect misfit in the bulk and cohesion enhancer at a grain boundary, Phys. Rev. B **77**, 165413 (2008).
[76] P. J. Steinhardt, D. R. Nelson, and M. Ronchetti, Bond-orientational order in liquids and glasses, Phys. Rev. B **28**, 784 (1983).
[77] G. Voronoi, Nouvelles applications des paramètres continus à la théorie des formes quadratiques. Deuxième mémoire. Recherches sur les parallélloèdres primitifs., J. Reine Angew. Math. **1908**, 198 (1908).
[78] Z. Huang, P. Wang, F. Chen, Q. Shen, and L. Zhang, Understanding solute effect on grain boundary strength based on

atomic size and electronic interaction, Sci. Rep. **10**, 16856 (2020).

[79] J. D. Rittner and D. N. Seidman, Solute-atom segregation to ⟨110⟩ symmetric tilt grain boundaries, Acta Mater. **45**, 3191 (1997).

[80] P. Käshammer and T. Sinno, A mechanistic study of impurity segregation at silicon grain boundaries, J. Appl. Phys. **118**, 095301 (2015).

[81] D. Scheiber, V. I. Razumovskiy, P. Puschnig, R. Pippan, and L. Romaner, *Ab initio* description of segregation and cohesion of grain boundaries in W–25 at.% Re alloys, Acta Mater. **88**, 180 (2015).

[82] S. Menon, G. Díaz Leines, and J. Rogal, pyscal: A python module for structural analysis of atomic environments, J. Open Source Softw. **4**, 1824 (2019).

[83] B. Ziebarth, M. Mrovec, C. Elsässer, and P. Gumbsch, Interstitial iron impurities at grain boundaries in silicon: A first-principles study, Phys. Rev. B **91**, 035309 (2015).

[84] D. Zhao and Y. Li, Revealing the factors influencing grain boundary segregation of P, As in Si: Insights from first-principles, Acta Mater. **168**, 52 (2019).

[85] J. P. Buban, K. Matsunaga, J. Chen, N. Shibata, W. Y. Ching, T. Yamamoto, and Y. Ikuhara, Grain boundary strengthening in alumina by rare earth impurities, Science **311**, 212 (2006).

[86] S. Fabris and C. Elsässer, First-principles analysis of cation segregation at grain boundaries in α-Al_2O_3, Acta Mater. **51**, 71 (2003).

[87] J. Chen, Y. N. Xu, P. Rulis, L. Ouyang, and W. Y. Ching, *Ab initio* theoretical tensile test on Y-doped $\Sigma = 3$ grain boundary in α-Al_2O_3, Acta Mater. **53**, 403 (2005).

[88] C. L. Briant, On the chemistry of grain boundary segregation and grain boundary fracture, Metall. Trans. A **21**, 2339 (1990).

[89] R. P. Messmer and C. L. Briant, The role of chemical bonding in grain boundary embrittlement, Acta Metall. **30**, 457 (1982).

[90] B. W. Krakauer and D. N. Seidman, Absolute atomic-scale measurements of the Gibbsian interfacial excess of solute at internal interfaces, Phys. Rev. B **48**, 6724 (1993).

[91] P. Maugis and K. Hoummada, A methodology for the measurement of the interfacial excess of solute at a grain boundary, Scr. Mater. **120**, 90 (2016).

[92] M. Nord, E. Vullum, I. Maclaren, T. Tybell, and R. Holmestad, ATOMAP: A new software tool for the automated analysis of atomic-resolution images using two-dimensional Gaussian fitting, Adv Struct Chem Imag **3**, 9 (2017).

[93] T. Malis, S. C. Cheng, and R. F. Egerton, Eels log-ratio technique for specimen-thickness measurement in the tem, J. Electron Microsc. Tech. **8**, 193 (1988).

[94] J. Madsen and T. Susi, The abTEM code: Transmission electron microscopy from first principles, Open Res. Eur. **1**, 13015 (2021).